RESEARCH PAPER

Correlation of ferrite formation to creep properties of Cr-Mo steel welds

Henry Granjon prize 2013 winner category B: materials behaviour and weldability

Xinghua Yu

Abstract A factor of four decreases from 16.0×10^{-4} to 4.1×10^{-4} %/h in steady state creep rate was observed in the fine-grained heat-affected zone (FGHAZ) of a Cr-Mo steel weld, by reducing the pre-weld tempering temperature from 760 to 650 °C. The current study used electron backscatter diffraction and synchrotron x-ray diffraction techniques to characterize the microstructure in the FGHAZ of the two tempering temperature conditions. The results showed carbide-free ferrite that formed in the FGHAZ of weldments that were pre-weld tempered at 760 °C, contributed to void formation resulting in lower creep strength. It is proposed that the formation of ferrite in the FGHAZ is due to the incomplete dissolution of $Cr_{23}C_6$ carbide at heating process during welding, which results in Cr enrichment adjacent to the undissolved $Cr_{23}C_6$ carbide. Dictra simulation confirmed ferrite formation at the carbide/austenite boundaries during $Cr_{23}C_6$ carbide dissolution.

Doc. IIW-2512, recommended for publication by Commission IX "Behaviour of Metals Subjected to Welding."

X. Yu (✉)
Department of Materials Science and Engineering,
The Ohio State University, Columbus, OH, USA
e-mail: xhyu.hit@gmail.com

X. Yu
Materials Science and Technology Division, Oak Ridge National Laboratory, Oak Ridge, TN, USA

1 Introduction

Cr-Mo steels, also known as creep strength enhanced ferritic (CSEF) steels, are widely used in fossil fuel power plants worldwide [1]. The creep resistance of CSEF steel welds, however, is not as good as the base metal. There have been many reports of failures at welded joints after only a few years of high-temperature service [2–4]. These failure locations are often traced back to the fine-grained heat-affected zone (FGHAZ) of the weld, which experiences a weld thermal cycle with a peak temperature just above the A_{c3} temperature. It is a well-established fact that non-equilibrium microstructure and their gradients in the FGHAZ region will significantly reduce creep strength [5–8]. Moreover, the size and orientation of the FGHAZ can lead to high tri-axial stress states that may contribute to accelerated creep damage [9, 10]. This combination of circumstances leading to premature failure of welded components is discussed in the literature as "type-IV failures in CSEF steels." The published literature also indicates that the creep strength reduction of such joints can be on the order of 40 % compared to base metal [11] for the same service life. Yu et al. [12] reported that creep resistance of welded grade 91 steel (A CSEF steel) can be improved greatly when a non-standard pre-weld temper is applied. Samples tempered at 650 °C (non-standard) prior to welding resulted in five times longer creep-rupture life during creep testing at 650 °C, with a stress level of 70 MPa, than in samples that were pre-weld-tempered at 760 °C (standard). Microstructural analysis showed type IV failure in both conditions. Coarse $M_{23}C_6$ carbide in the FGHAZ was responsible for the low creep strength in the standard pre-weld temper condition. Detailed examination revealed a small amount of carbide-free ferrite had formed in the FGHAZ of the standard condition, but not in the non-standard condition. This carbide-free ferrite is now being considered as a contributor to type IV failure in the FGHAZ.

Several mechanisms of type IV failure have been proposed. At the microstructure level, coarse carbides at ghost austenite grain boundaries (prior austenite grain boundaries in the base materials) have been shown to be responsible for low creep strength in the FGHAZ [13, 14]. Coarse carbides also accelerate the formation of Z-phase, which is detrimental to the creep strength of a cross-weld sample [15]. In addition, finite element modeling of cross-weld samples with inhomogeneous microstructures pointed to strain mismatch and tri-axial stresses generated in the FGHAZ, which accelerate creep void formation [16]. When the stress level is low, grain boundary sliding becomes the major deformation mechanism and promotes initiation of voids on the grain boundaries lying approximately normal to the tensile axis. Kimmins and Smith simulated creep behavior of a cross-weld sample by allowing grain boundary sliding and found failure in the FGHAZ was due to the high constraint that was relaxed by grain boundary sliding [17].

A new mechanism for type IV failure is proposed in the current study. First, carbide-free ferrite forming in the FGHAZ after welding, near undissolved carbides; then, due to the low creep resistance of carbide-free ferrite, creep voids are initiated in the ferrite during the early stage of creep deformation. The voids lead to pre-mature failure in the FGHAZ. Different in situ and ex situ techniques were used to confirm the formation of carbide-free ferrite. One of the in situ techniques to measure phase transformation was time-resolved x-ray diffraction (TRXRD). TRXRD is capable of characterizing the volume fraction of phases and the lattice parameter as a function of imposed thermal cycles. In the past decade, synchrotron-based in situ TRXRD systems have been used extensively to investigate phase transformations in steels [18–24]. Microstructure evolution and quantitative analysis of $M_{23}C_6$ and MX in stainless steel [25–31] and 2.25Cr-1Mo steels [32, 33] has been extensively studied using conventional XRD. However, the amount of ferrite formed in grade 91 steels is very small, and it is difficult to detect with conventional laboratory x-ray sources. Therefore, the TRXRD technique with high-flux synchrotron radiation was adopted to characterize the samples undergoing typical HAZ thermal cycles. Samples subjected to HAZ simulation were also examined by electron backscattering diffraction technique to confirm the existence of ferrite. Ferrite formation was also confirmed using simulations in Dictra.
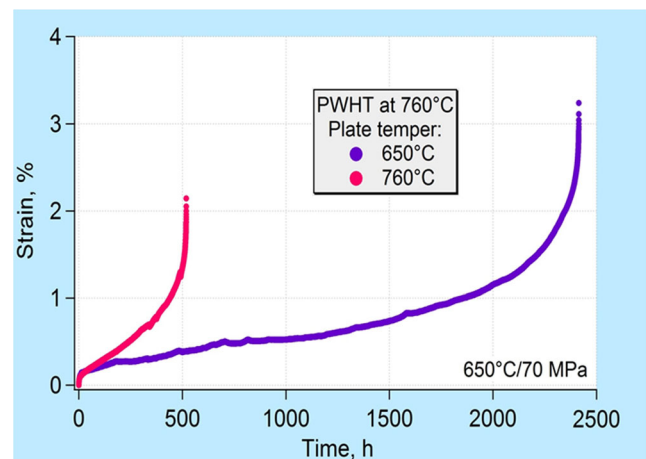

Fig. 1 Creep curves for welded samples with different pre-weld tempering temperature [12]

## 2 Experimental

2.1 Steels and welding

The chemical composition of ASTM Grade 91 (heat number 30176) is shown in Table 1. The material was cast and then thermomechanically processed in the rolling mill. The steel plates were then austenitized in an argon atmosphere furnace at a temperature of 1080±2 °C for 2.5 h and air cooled. Two tempering temperatures were investigated in the current study: 760 and 650 °C. The samples were tempered in an argon atmosphere furnace for 1.5 h followed by air cooling to room temperature. Unless otherwise noted, these conditions are designated as "standard" (760 °C) and "non-standard" (650 °C) throughout the text. These two base materials with different pre-weld tempering conditions were used for welding and simulated weld thermal cycling experiments.

Two 0.5-in. plates, in the standard and non-standard condition, were machined on the edge with an angle of 37.5° to make a single-V groove weld. The plates were pre-heated to 125±2 °C before welding. Automated gas tungsten arc welding (GTAW) was performed on the plates with one root pass and six fill passes while protecting the weld from oxidation with argon cover gas. Welding current, voltage, travel speed, and wire feed rate were kept constant at 260 A, 8 V, 2.5 mm/s, and 59 mm/s, respectively, to maintain a calculated constant heat input of 0.33 MJ/m. A 9Cr-1Mo filler wire 1.6 mm in diameter was used. The welded plates were

Table 1 Chemical composition (wt.%) of heat 30176 grade 91 steel

C	Mn	P	S	Si	Cr	Mo
0.081	0.37	0.01	0.003	0.11	8.61	0.89
Ni	V	Nb	N	Al	Ti	Zr
0.09	0.2	0.072	0.055	0.007	0.002	0.001

Table 2 Summary of creep test results

Tempering temperature (°C)	Primary creep strain (%)	Steady state creep rate (10^{-4} %/h)	Total strain (%)	Test time (h)
650	0.21	4.1	3.24	2414
760	0.08	16	2.14	518

Fig. 2 **a** SEM image of FGHAZ in standard after creep test and **b** SEM image of FGHAZ in non-standard after creep test [12]
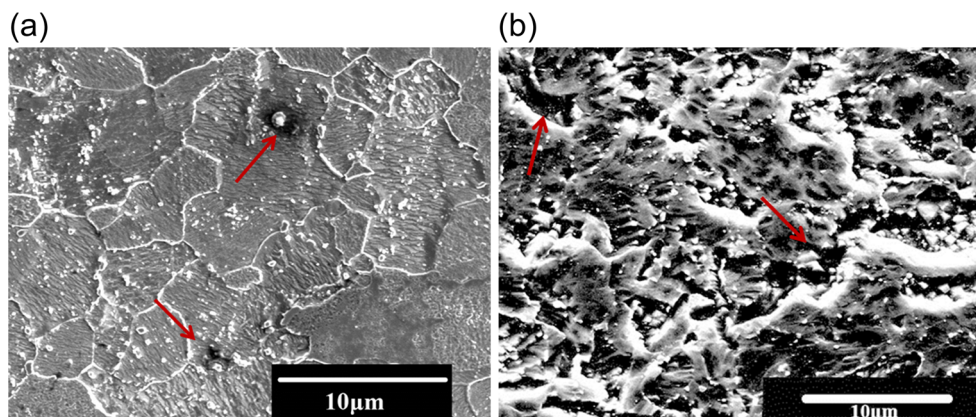
post-weld heat-treated (PWHT) in an air atmosphere furnace at 760±2 °C for 4 h followed by air cooling to room temperature. After PWHT, the plates were sectioned and creep samples machined.

2.2 Creep testing

Tensile creep-rupture tests of the welded plates were performed according to ASTM Standard E139-06 [34]. Lever-arm creep machines were calibrated to a load accuracy of ±0.5 %. The temperature was measured by three Chrome1 vs. Alumel thermocouples (±0.4 % accuracy) wired to the gage section. The temperature variation among these was less than 1.0 °C, and the highest temperature was taken as the nominal test temperature. Constant loading creep-rupture tests were performed at 650 °C with an initial stress of 70 MPa (10 ksi). A proportioning temperature controller was used to maintain ±1.0 °C. Length change was measured by an averaging extensometer attached by set screws to a small groove in the specimen shoulder. The displacement reading was

converted to strain by dividing by the reduced section length. The dial gage used in measuring the extension had a resolution of 2.5 μm. The strain was recorded every 36 s during the first 37 min, then every 360 s until test termination.

2.3 Ex situ characterization

2.3.1 Extraction replica and transmission electron microscopy

Microscopy samples were polished and then etched by Fry's reagent. As a result, carbides were exposed on the surface. A thin layer of carbon film was deposited on the etched sample surface by electro-spark coating. Squares of 2–3 mm in size were cut from the carbon film with a razor blade to excise the replica. The sample was then soaked in 50 % hydrochloric acid (HCl) for approximately 1 h to debond the carbon replica. After the HCl soak, the samples were put into water to allow the replicas to float. A 3-mm Cu grid was used to hold the carbon replicas for TEM examination.
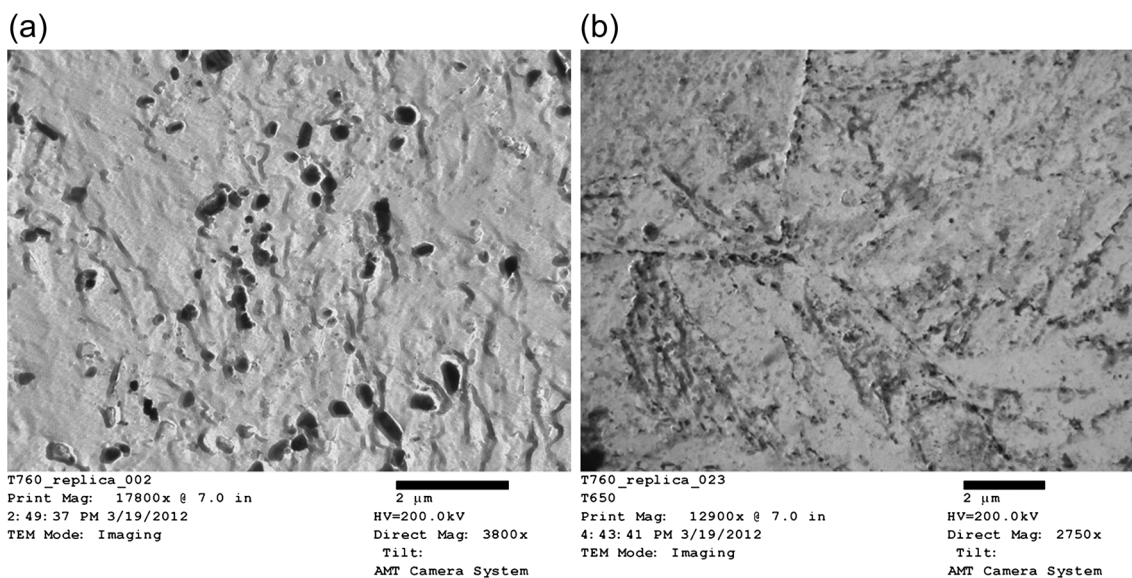

Fig. 3 Microstructure of pre-weld tempered samples. **a** SEM images for standard and **b** non-standard

A Philips CM-200 TEM operated at 200 kV accelerating voltage was used to study the carbides. The composition analysis was achieved by the EDAX energy dispersive x-ray spectrometer (EDS). A spot size of 200 nm was used, as this size utilizes a lower amount of beam current, hence, lowering the x-ray dosage to the detector. The lower beam current results in a higher accuracy. Carbides identified in the photographs of the current study
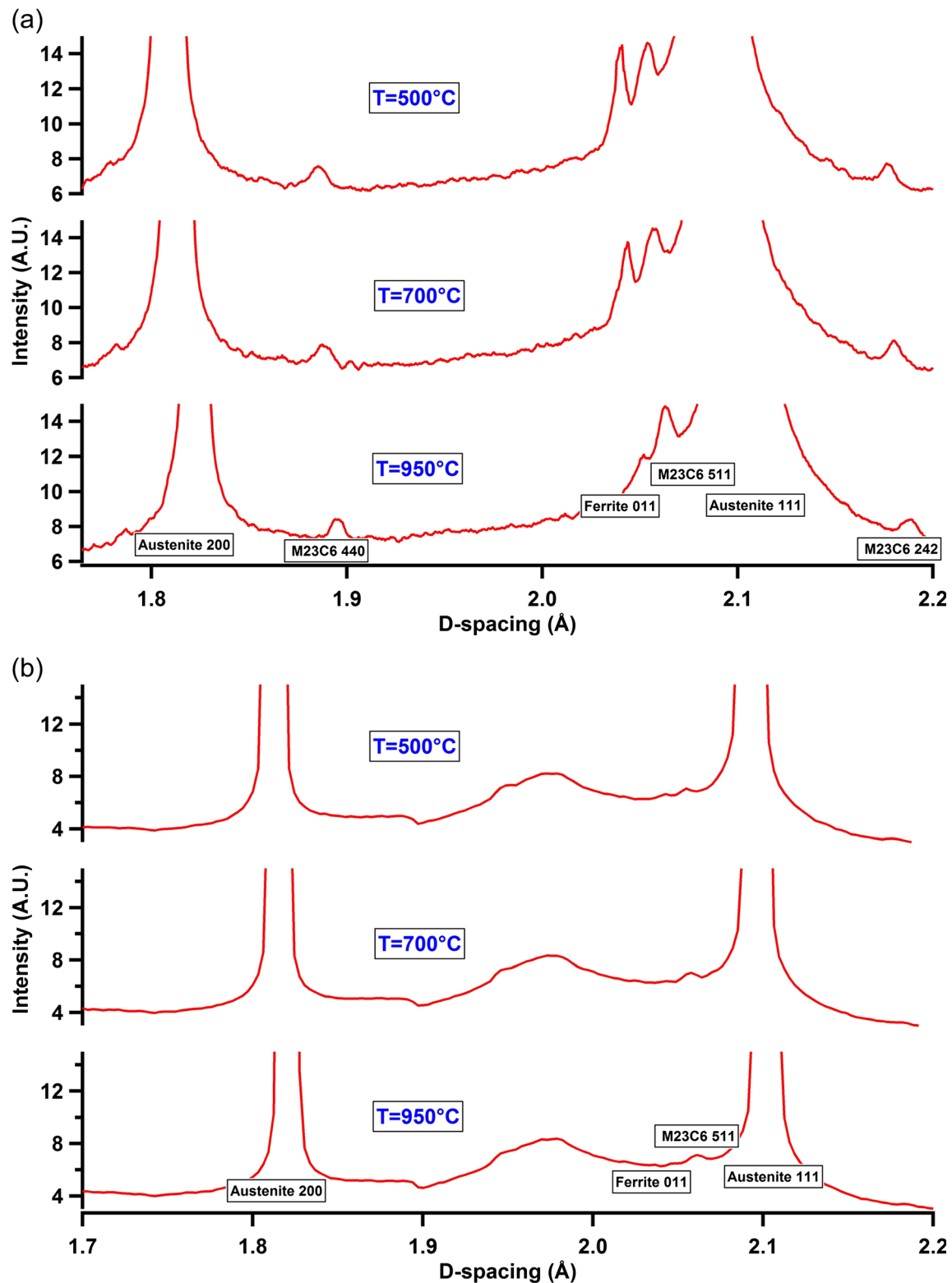

Fig. 4 Diffraction result as a function of time and temperature in FGHAZ (Tp=950 °C) for **a** standard and **b** non-standard

have been confirmed by EDS and selected area diffraction (SAD).

2.3.2 Scanning electron microscopy

A Philips ESEM FEG-30 scanning electron microscope (SEM) equipped with an EDAX® TSL electron back-scattered diffraction (EBSD) detector was used. Samples for SEM and EBSD were grinded and polished with a finishing of 0.2-μm colloidal silica. SEM secondary electron images were taken at an accelerating voltage of 20 kV and spot size of 5 nm. The working distance was set at 10 mm.

2.4 In situ characterization

2.4.1 Time-resolved x-ray diffraction with synchrotron radiation

An in situ characterization system was used to observe phase transformations in these steels. The system has been discussed elsewhere [21, 33]. Disk-shaped samples were prepared 5 mm in diameter by 2 mm in height. The in situ observation system was situated within a 46XU beamline at Spring-8 in Hyogo, Japan. The infrared furnace was set on the theta-axis of the goniometer. Samples were placed inside a boron nitride (BN) crucible, which was held by a platinum holder with a type K thermocouple (±9 °C accuracy at 1200 °C) attached to measure temperature and thereby control the heat flux generated by the halogen lamps. The sample was placed at the focal point of the halogen lamp and mirror systems. During the experiments, the furnace was filled with pure argon (99.99996 %) after evacuation to prevent sample oxidation. The current work showed a small temperature gradient under rapid heating/cooling conditions from the top surface (where was measured by x-ray) to the bottom (where the thermocouple is attached) of the sample, a correction factor was used to account for these gradients. A large-area pixel detector, Pilatus 2M [35], was placed on the 2-theta axis. The incident beam (30 keV) was focused on the sample surface, and the resulting diffraction rings were recorded by the pixel detector. The time resolution dictated by the detector hardware was 0.3 s. The x-ray wavelength was set at 0.413269 Å. A 5°glancing angle of the beam on the sample surface of lead to a total irradiated area on the sample surface of 2.07 mm^2. The depth of x-ray interaction in the sample was estimated to be 16 μm [18]. Peak temperature of simulated FGHAZ is 950 °C,

Fig. 5 a EBSD map and b image quality map of FGHZA in the standard sample; c EBSD map and d image quality map of FGHZA in the non-standard sample
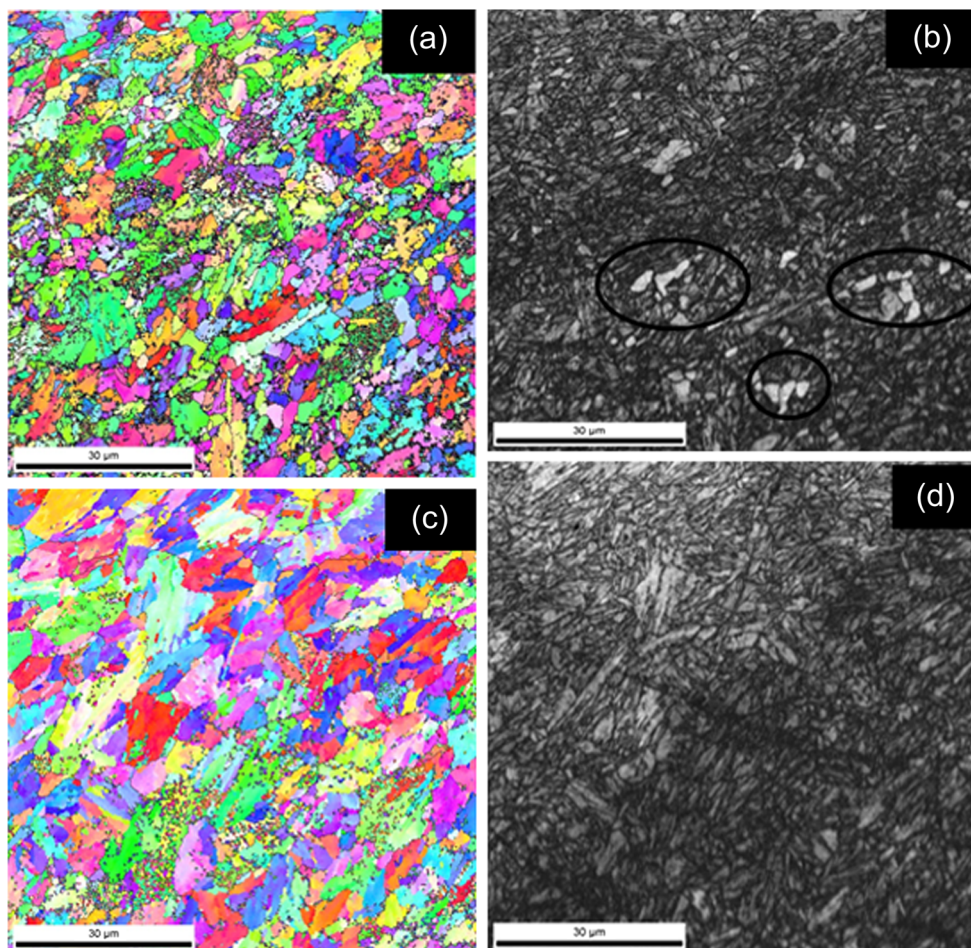
and both heat rate and cooling rate are 10 °C/s. The diffraction rings on each image were integrated to give one-dimensional scans of intensity vs. inter-planar spacing [36, 37]. The diffraction data were then synchronized with measured thermal cycles. The scans were analyzed using an automatic peak fitting algorithms. The methodology is described in the published literature [19, 21].

3 Results and discussion

3.1 Creep rates and microstructure

The strain vs. time curves for creep-rupture tests (at 650 °C with a 70 MPa stress) are shown in Fig. 1 [12]. The creep test results were further analyzed and summarized in Table 2. According to the ASTM 387 specification for grade 91 steel, the temperature range for pre-weld temper is 730–790 °C. Therefore, the pre-weld temper of 760 °C (standard) in the current experiments represents the conditions of industrial practice. However, the creep curves in Table 2 reveal that the non-standard sample with a 650 °C pre-weld temper has a lower steady state creep rate and a 5 times longer creep life than the standard sample. Yamamoto et al. [38] also reported that non-standard heat treatment had three times longer creep life than standard heat treatment when samples were tested at 600 °C with a 100 MPa. It is noted here that the life of power plant grade 91 components usually exceed 200,000 h. Parametric approaches can be used in order to extrapolate short-term lab creep tests to service lives [39].

Figure 2 [12] shows the cross-sectional microstructures at the FGHAZ of the creep-ruptured samples. The microstructure of both samples shows equiaxed ferrite grains with creep voids on grain boundaries. The formation of equiaxed ferrite from the original tempered lath martensite is a well-known phenomenon [40]. In the standard sample (Fig. 2a), carbide clusters are highlighted by circles. In the non-standard sample, a uniform dispersion of fine carbides is seen instead of carbide clusters (Fig. 2b). In addition, creep voids in the standard sample were found adjacent to the coarse carbides while voids in the non-standard sample were only found at grain boundaries (indicated by arrows). Based on these results in the current study, it is hypothesized that the creep voids in the standard sample are due to the low creep strength of the ferrite that formed adjacent to the coarse carbides in the FGHAZ. Formation of ferrite is confirmed with time-resolved x-ray diffraction, electron microscopy, and thermodynamic and kinetic modeling.

3.2 Microstructure after pre-weld tempering

In order to understand the improvement in creep properties of the non-standard sample, the microstructure of the pre-weld

conditions were investigated. Figure 3a (non-standard) and 3b (standard) show TEM images of carbides in the tempered samples prior to welding. Since carbides tend to form at prior austenite grain boundaries (PAGBs) and martensite block boundaries, and those boundaries are usually straight, the presence of carbides in a straight line suggests the presence of those boundaries. Potential boundaries (prior austenite grain boundaries or martensite block boundaries) are indicated by dashed lines (see Fig. 3a, b). Two types of carbides, $M_{23}C_6$ (M = Cr, Fe) and MX (M = Nb, V; X = C, N), were confirmed by EDS and SAD. Sizes, of the $M_{23}C_6$ were determined by a random mean intercept method on the TEM images. The average diameter of the $M_{23}C_6$ in the standard sample was 164.0±24.6 nm, compared to 76.7±10.7 nm in the non-standard sample.

Since the creep failure occurred in the FGHAZ, it was necessary to discern the carbide distribution and morphology in three conditions: pre-weld temper, post-weld, and post-weld temper. Due to the steep temperature gradients in welds and the narrow zone of interest, extraction of sufficient material to perform testing on the FGHZ extracted directly from weldments was impractical. Therefore, for in situ characterization studies, large-scale non-standard and standard samples were produced and subjected to weld thermal cycles typical of the FGHAZ.

Figure 4 presents the diffraction data with d-spacing from 1.7 to 2.2 Å at 950, 700, and 500 °C for standard (Fig. 4a) and
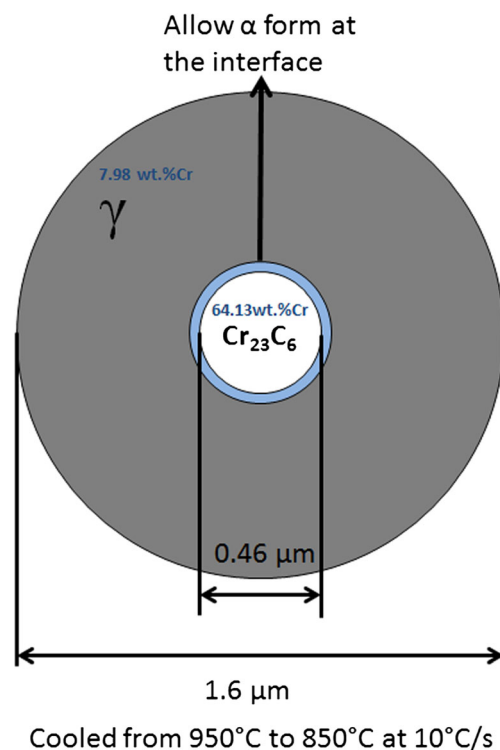

Fig. 6 Schematic of Dictra model showing dissolution of M23C6 and formation of ferrite

non-standard (Fig. 4b) samples on cooling. Six diffraction peaks: ferrite (011), austenite (200), austenite (111), $M_{23}C_6$ (440), $M_{23}C_6$ (511), and $M_{23}C_6$ (242) were indexed. For the standard sample at 950 °C, x-ray diffraction revealed an austenite matrix with a small fraction of $M_{23}C_6$. The intensity of the ferrite (011) peak is quite close to the background, indicating nearly 100 % transformation from ferrite to austenite at the peak temperature. When the sample was cooled to 700 °C, a small ferrite (011) peak was revealed, indicating ferrite formation prior to 700 °C. As the temperature decreased from 700 to 500 °C, the intensity of the ferrite peak increased. The onset of the martensite transformation was 420 °C. Quantitative analysis on the phase fractions showed that $M_{23}C_6$ was reduced from 1.6 to 0.9 vol.% during heating and maintained at 0.9 vol.% during cooling. The ferrite that formed at 700 and 500 °C was 0.15 and 0.35 vol.%,

respectively. Ferrite peaks were absent in the non-standard sample during cooling. Intensities of the $M_{23}C_6$ peaks were extremely close to background and could not be quantified.

A post-thermal treatment EBSD investigation was performed, and results are shown in Fig. 5. The image quality map of the standard sample subjected to the FGHAZ thermal cycle reveals regions with high image quality (indicated by the arrows). Since martensite has a high density of dislocations, image quality is usually low. High-image quality regions represent polygonal ferrite. These ferrite grains are clustered in specific boundaries (prior austenite grain boundaries or martensitic sub-boundaries), which have a high density of carbides. The non-standard FGHAZ samples show only a martensitic microstructure, in agreement with TRXRD results. The current study proposes that the ferrite formation in the

Fig. 7 Dictra simulation results **a** ferrite and $M_{23}C_6$ weight fraction as a function of time and **b** Cr concentration profile at 950, 949, and 850 °C. A 0.46 μm diameter spherical $Cr_{23}C_6$ in a 1.6 μm diameter austenite matrix. Composition of Cr is as indicated.
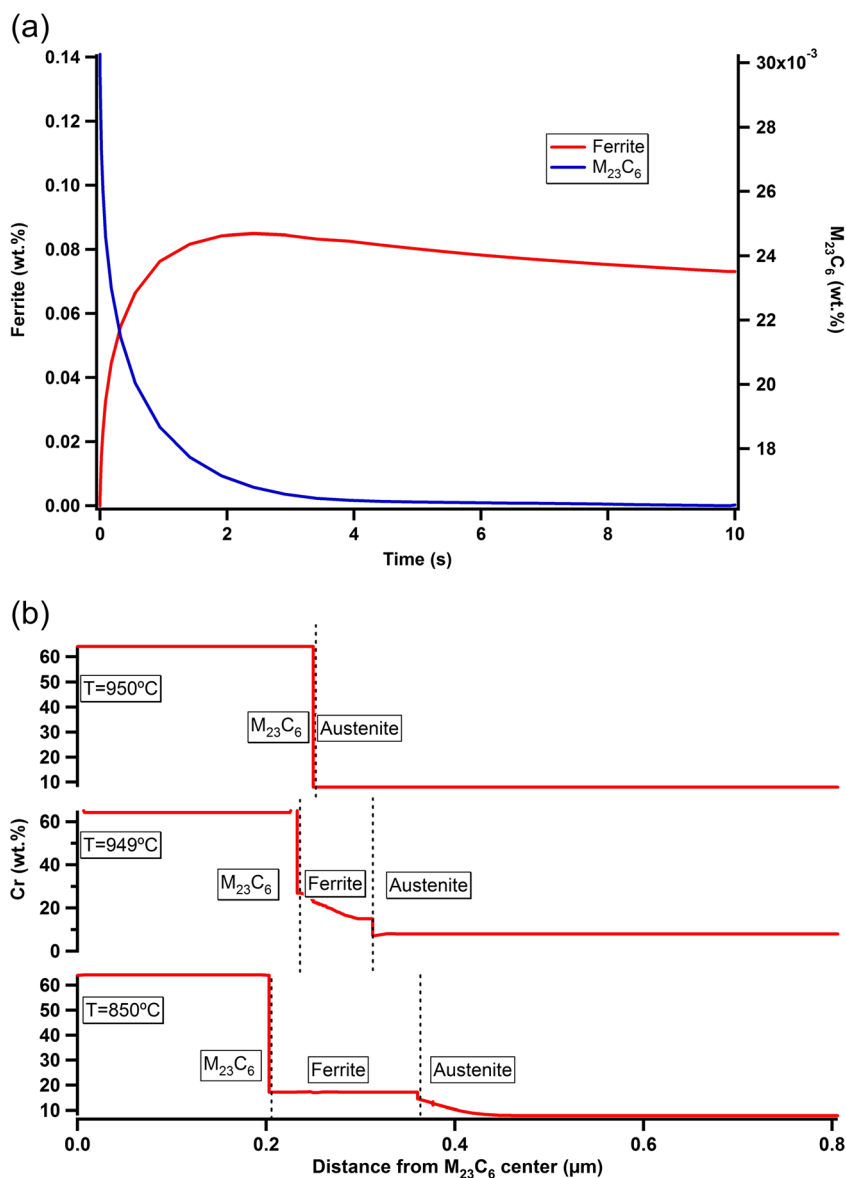
standard FGHAZ sample is associated with dissolution of large Cr-enriched $M_{23}C_6$ carbides.

Thermo-Calc® predicted that dissolution of $M_{23}C_6$ carbide occurred mainly in austenite matrix. Ac_3 and M_s measured from TRXRD for current Grade 91 steel are 820 and 410 °C, respectively. As a result, time for carbide dissolution during cooling is much longer than that during heating. To simplify the model, the current simulation only considered on cooling. The dissolution of $M_{23}C_6$ carbide and ferrite formation phenomenon was simulated by thermodynamic and kinetic modeling using Dictra® software. The schematic of the model is shown in Fig. 6. Spherical $M_{23}C_6$ (Fe-64.13wt.%Cr-5.56wt.%C) with a diameter of 0.46 μm in an austenitic (γ) matrix (Fe-7.98wt.%Cr-0.0039C) was cooled from 950 °C at 10 °C/s. The austenite to ferrite (α) phase transformation was allowed at the carbide/austenite interface. Unfortunately, due to fatal integration errors, the simulation crashed at $t=10s$ ($T=850$ °C). However, the model still successfully predicted reactions, including carbide dissolution and austenite to ferrite transformation. Figure 7a shows the weight fraction of the $M_{23}C_6$ and ferrite as a function of time when the system was cooled from 950 to 850 °C. The model predicted that the dissolution of $M_{23}C_6$ would occur immediately at 950 °C. With the dissolution of $M_{23}C_6$, the weight fraction of ferrite also increased. The Cr composition profiles at 950, 949 ($t=0.1$ s to verify if ferrite formed immediately during cooling), and 850 °C are plotted in Fig. 7b. When $M_{23}C_6$ is dissolving, both Cr and C are diffused into austenite. The solubility of Cr in austenite is low (less than 13 % according to the thermodynamic calculation). As a result, Cr accumulates at the carbide austenite interface. Austenite with a high Cr concentration will transform to ferrite since Cr is a significant ferrite stabilizer. Since austenite has a high solubility of C and it diffuse much faster, effect of C on ferrite formation can be ignored.

Since the austenite to ferrite transformation is reconstructive, there is no carbon supersaturation in ferrite. Consequently, ferrite will be carbide-free after post-weld heat treatment. Ferrite will significantly decrease the creep strength of Grade steel [41, 42]. In the non-standard condition, since the amount of $M_{23}C_6$ carbide is low, complete dissolution of $M_{23}C_6$ is expected during welding, with no significant Cr enrichment in austenite adjacent to the dissolved carbides. As a result, the occurrence of ferrite formation in the non-standard treatment is low, resulting in good creep resistance.

4 Conclusion

The current study shows that the pre-weld tempering temperature has a significant impact on the creep behavior of a grade 91 Cr-Mo steel-welded structure. Creep failure was observed in the FGHAZ, and the microstructure evolution was characterized using ex situ and in situ techniques.

Creep life of welds on plate where the pre-weld temper was 650 °C (non-standard) was five times higher than that of welds where the pre-weld temper was 760 °C (standard). Detailed microstructure characterization indicated that the differences in the creep properties were correlated with ferrite formation.

TRXRD experiments revealed a small amount of ferrite formed in the FGHAZ simulation of the standard (760 °C pre-weld temper) condition. In contrast, the ferrite formation in the FGHAZ simulation of the non-standard (650 °C pre-weld temper) condition was very small and inconsequential.

EBSD results showed polygonal ferrite in clusters in the standard FGHAZ, but no ferrite appeared in the non-standard FGHAZ. It is hypothesized that ferrite is formed due to partial dissolution of $M_{23}C_6$ resulting in an accumulation of Cr near undissolved $M_{23}C_6$.

Dictra simulation showed ferrite formed at the austenite/carbide interface because of the dissolution of Cr enriching the adjacent austenite.

References

1. Bhadeshia HKDH (2001) ISIJ Int 41:626
2. Henry JF (2005) Combined Cycle J 8
3. I.A. Shibli, K. Coleman, www.ommi.co.uk/etd/ETD-EPRI-%20P91%20Failures.pdf
4. Berte FJ (2007) Combined Cycle J 52
5. Francis JA, Mazur W, Bhadeshia HKDH (2006) Mater Sci Technol 22:1387
6. Abe F, Tabuchi M (2004) Mater Sci Technol 9:22
7. Hirata H, Ogawa K (2005) Weld Int 19:37
8. Hirata H, Ogawa K (2005) Weld Int 19:118
9. Albert SK, Matsui M, Watanabe T, Hongo H, Kubo K, Tabuchi M (2003) Int J Press Vessel Pip 80:405
10. Li D, Shinozaki K, Kuroki H (2003) Mater Sci Technol 19:1253
11. Otoguro Y, Matsubara M, Itoh I, Nakazawa T (2000) Nucl Eng Des 196:51
12. Yu X, Babu SS, Terasaki H, Komizo Y, Yamamoto Y, Santella ML (2013) Acta Mater 61:2194
13. Yu X, Santella ML, Yamamoto Y, Terasaki H, Komizo Y, Babu SS (2014) In situ phase transformation study in fine grained heat affected zone of grade 91 steels. In in situ Studies with photons, neutrons and

electrons scattering II. Springer International Publishing, Switzerland, pp 29–49

14. Yu X, Babu SS, Terasaki H, Komizo Y, Yamamoto Y, Santella ML (2013) Correlation of precipitate stability to increased creep resistance of Cr–Mo steel welds. Acta Mater 61(6): 2194–2206
15. Letofsky E, Cerjak H (2004) Metallography of 9Cr steel power plant weld microstructures. Sci Technol Weld Join 9(1):31–36
16. Li D, Shinozaki K, Kuroki H (2003) Stress–strain analysis of creep deterioration in heat affected weld zone in high Cr ferritic heat resistant steel. Mater Sci Technol 19(9):1253–1260
17. Kimmins ST, Smith DJ (1998) On the relaxation of interface stresses during creep of ferritic steel weldments. J Strain Analysis Eng Des 33(3):195–206
18. Elmer JW, Wong J, Ressler T (2000) Scripta Mater 43:751
19. Babu SS, Elmer JW, Vitek JM, David JM (2002) Acta Mater 50:4763
20. Wong J, Ressler JW, Elmer J (2003) Synchrotron Radiat 10:154
21. Babu SS, Specht ED, David SA, Karapetrova E, Zschack P, Peet M, Bhadeshia HKDH (2005) Metall Mater Trans A 36A:3281
22. Stone HJ, Peet MJ, Bhadeshia HKDH, Withers PJ, Babu SS, Specht ED (2009) Proc Roy Soc A 464:1009
23. Offerman SE, van Dijk NH, Sietsma J, Grigull S, Lauridsen EM, Margulies L, Poulsen HF, Rekveldt MT, vander Zwaag S (2002) Science 298:1003
24. Terasaki H, Komizo Y (2011) Scripta Mater 64:29
25. Rozenak P, Eliezer D (1986) J Mater Sci 21:3065
26. Lai JKL, Galbraith IF (1980) J Mater Sci 15:1297
27. Terao N, Sasmal B (1980) Metallography 13:117
28. Parish C, Watkins T, Rios O, Mackiewicz-Ludtka G, Ludtka G, Cavin O (2011) Microsc Microanal 17:410
29. Beneteaua A, Weisbeckera P, Geandierb G, Aeby-Gautiera E, Appolaire B (2005) Mater Sci Eng A 393:63
30. Yonemura M, Osuki T, Hirata H, Ogawa K (2008) Metall Mater Trans A 39A:113
31. Zhang XF (2012) Scripta Mater. doi:10.1016/j.scriptamat.2012.04.019
32. Stevens RA, Lonsdale D (1985) J Mater Sci 20:3631
33. Mitchell DRG, Ball CJ (2001) Mater Charact 47:17
34. ASTM Specification A139-06 (2008) Section II, part A
35. Broennimann C, Eikenberry EF, Henrichn B, Horisberger R, Huelsen G, Pohl E, Schmitt B, Schulze-Briese C, Suzuki M, Tomizaki T, Toyokawa H, Wagner A (2006) The PILATUS 1M detector. J Synchrotron Radiat 13:120–130
36. Hammersley AP, Svensson SO, Hanfland M, Fitch AN, Hausermann D (1996) High Press Res 14:235
37. Hammersley AP (1997) ESRF Internal Report No. ESRF97HA02A. ESRF, Grenoble, Cedex, France
38. Yamamoto Y, Yu X, Babu SS (2014) Proceedings of the ASME Symposium on Elevated Temperature Application of Materials for Fossil, Nuclear, and Petrochemical Industries ASME (2014), S2-1 ETS 2014–1009
39. Evans M (2008) J Mater Sci 43:6070
40. Hasegawa Y, Muraki T, Ohgami M (2004) Metallurgical investigation of a type IV damage at the heat affected zone of weld for tungsten containing martensitic heat resistant steels', in International Conference Experience with Creep-Strength Enhanced Ferritic Steels and New and Emerging Computational Methods, ASME, San Diego
41. Masuyama F (2001) ISIJ Int 41:612–625
42. Tsuchida Y, Tokuno K, Hashimoto K (1993) Nippon Steel Technical Report No 58:27–35